# Charge-Based Droop Control Addressing Control Saturation for Low-Inertia Converters


Zheng An
School of Electrical and Computer Engineering
Georgia Institute of Technology
Atlanta, GA, USA
zheng.an@gatech.edu

Rajendra Parasad Kandula
Oak Ridge National Laboratory
Oak Ridge, TN, USA
krprasad@gmail.com

Joseph Benzaquen
School of Electrical and Computer Engineering
Georgia Institute of Technology
Atlanta, GA, USA
jbenzaquen@gatech.edu

Deepak Divan
School of Electrical and Computer Engineering
Georgia Institute of Technology
Atlanta, GA, USA
ddivan@gatech.edu



***Abstract*—With bulky dc-link capacitors/inductors, traditional voltage-source converters (VSCs) and current-source converters (CSCs) feature a large inertia to facilitate the converter control under large transients. To achieve high power density with reduced cost, low-inertia converters (LICs) featuring significantly reduced dc-link capacitors/inductors have attracted growing attention. However, without bulky dc-link energy buffer, LICs are prone to control saturation under large transients, resulting in undesired oscillation and instability. This issue cannot be managed by traditional proportional-integral based control due to the low inertia. And it will deteriorate when several LICs are connected in series. To address this challenge in LICs, a model-predictive control (MPC) with a computation-inexpensive feed-forward compensation method has been proposed to provide fast dynamic responses. But it would suffer control saturation under larger transients that degrades the control performance. In this article, a charge-based droop control (CDC) is proposed to address this remaining challenge. This paper firstly analyzes the control saturation challenge in LICs by using a tri-port soft-switching solid-state transformer as an example. Next, the operating principle of the proposed CDC are introduced. Two different implementation approaches are discussed in detail. Lastly, the proposed scheme is validated in simulation with a high-fidelity model of hardware prototype. The proposed CDC eliminated the 2 kHz oscillation and reduced the dc-link ripple and overshoot due to control saturation by 75% and 50%, respectively.**



***Keywords—Droop control, control saturation, current-source converters, soft-switching solid-state transformer, low inertia.***


## I. Introduction

With bulky dc-link capacitors or inductors, traditional voltage-source converters (VSCs) and current-source converters (CSCs) feature a large inertia as the energy buffer. This nature facilitates traditional proportional-integral (PI) based control, despite of its relatively slow dynamics, to respond to large transients effectively. But these bulky dc-link elements has become one of major barriers to high-power-density applications [1-3].

Compared with conventional converters with bulky dc-link capacitors or inductors, low-inertia converters (LICs) reduce the dc-link size significantly, leading to improved power density and decreased total cost. Hence, LICs have attracted growing attention in recent years and can be found in various applications, such as motor drives, solar inverters, solid-state transformers, and energy routers [4-10].


This work was supported by the U.S. DOE and the Center for Distributed Energy at Georgia Tech.


In [6], a single-stage soft-switching solid-state transformer (S4T) was proposed. It features a low-inertia current-source converters with universal interface of DC, single-phase AC, and three-phase AC. In addition, S4T converter also provides soft-switching operation across entire load range, bidirectional power flow capability, galvanic isolation, controlled low dv/dt and electromagnetic interference (EMI). However, similar to other LICs, owing to the absence of bulky dc-link energy buffer, LICs require a fast-response control to survive from large transients, making the traditional PI-based control a less competitive option to model-based control. In addition, once the transients go beyond the dc-link's operating range, LICs are prone to control saturation, resulting in undesired oscillation, power imbalance, and instability in the worst case. These issues become more challenging once LICs are connected in series stacked way [3, 11].

To address this challenge, a model-predictive priority-switching (MPPS) was proposed in [3]. It controls selected parameters based on the control priority during large transients due to limited control degree of freedom. But it is contrained by dc-link current overrating, resulting in control saturation. In addition, a second-order compensation would be computationally expensive when being applied to $N$-port LICs ($N \geq 3$). Instead, a new feed-forward compensation method with only one arithmethic operation was proposed in [11] to reduce implementation effort and computation cost, making it friendly to $N$-port LICs. However, the challenge of control saturation still remains during large transients. It leads to dc-link oscillation and in the worst case, even collapse due to the instability, requiring a dedicated scheme to enhance the reliability of LICs.

To address control saturation issue in LICs, a charge-based droop control (CDC) is proposed in this article. It features fast-response, easy implementation, high scalability, and no extra hardware components. Taking a S4T-based tri-port medium-voltage string inverter (TMVSI) as an example of LICs, an dc-link oscillation issue induced by control saturation is presented. Next, the proposed CDC and its two implementation approaches are introduced. Lastly, simulation results are exhibited to validate the effectiveness of the proposed scheme.

## II. Tri-Port Medium-Voltage String Inverter

Based on S4T topology, the tri-port medium-voltage string inverter (TMVSI) features a competitive candiate for utility-scale solar-plus-storage farms [7]. It integrates paired battery storage without adding extra converters and enable medium-

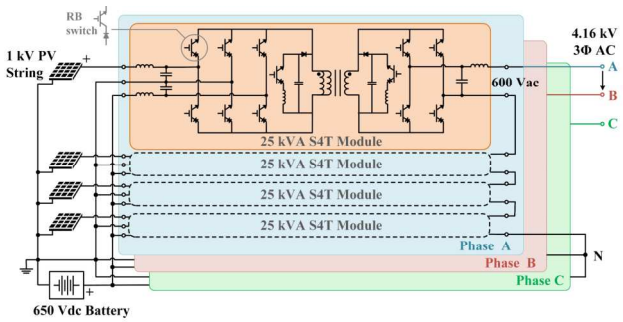


Fig. 1. Schematic of the 300 kVA/4 kVac S4T-based tri-port medium-voltage string inverter.

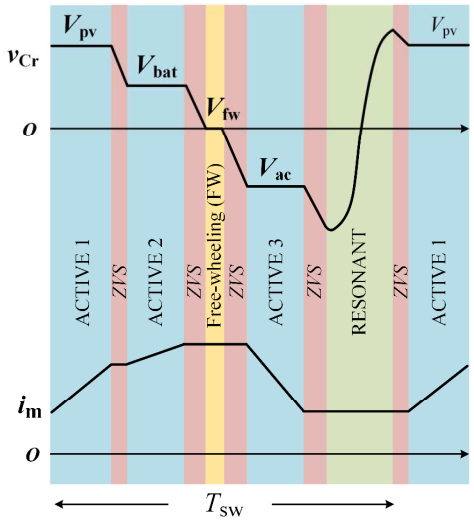


Fig. 2. Characteristic operating waveform of TMVSI. PV and battery charges dc-link magnetizing inductance while AC port discharges it.

voltage colletion network of photovoltaic (PV) energy to reduce copper cost and losses, leading to significantly reduced levelized cost of energy (LCOE) for utility-scale PV farms [12]. It also presents several other attractive features to leverage WBG devices, including soft-switching operation over the entire load range, fully bidirectional power flow capability, galvanic isolation, controlled low dv/dt and EMI, benign fault tolerance, and independent power flow control of different ports [6, 7]

Fig. 1 shows the schematic of 300 kVA/4 kVac S4T-based TMVSI. It contains twelve 25 kVA/600 Vac S4T modules connected in the input-parallel-output-series (IPOS) way. Each module is configured as a tri-port S4T to interface PV and battery storage on the low-voltage (LV) bridge. On the medium-voltage (MV) bridge, each module outputs a 600 V single-phase AC voltage for series stacking and four of them are connected in series to achieve 2.4 kVac MV on the AC side. Three of them with a 120° phase shift constitute a three-phase system to achieve 4 kV MVAC output. For each 25 kVA/600 Vac S4T module, it consists of two CSC bridges for input/output interface, a medium-frequency transformer (MFT) for galvanic isolation and energy storage, two auxiliary resonant tanks comprising active switches and LC circuits enabling zero-voltage-switching (ZVS) for main devices.

Fig. 2 presents characteristic waveforms of TMVSI [7]. Similar to traditional flyback converters, the active voltage vectors formed by input/output ports, $v_{\mathrm{pv}}, v_{\mathrm{bat}}, v_{ac}$, and a free-wheeling state, $v_{\mathrm{fw}}$, are connected to the MFT for a certain portion of switching cycles to transfer the power. These vectors are sorted in the descending order of their voltage magnitudes to guarantee ZVS conditions for main devices with the aid of resonant tanks. At the end of each switching cycle, the resonnat state will be activated to flip the resonant capacitor voltage, preparing the ZVS conditions for the next cycle. As a result, the dc-link magnetizing current of the MFT will vary during active states while remaining nearly constant during ZVS, freewheeling, and resonat state.

Please note that the MFT of the TMVSI usually features a several hundreds of microhenry, significantly smaller than traditional CSCs. A current ripple of 0.4 ~ 0.6 per unit (p.u.) is typically selected to provide control flexibity. Hence, only a small amount of energy can be stored in the reduced dc-link, featuring a low inertia nature. Differrent from traditional converters with bulky dc-links, the low inertia of TMVSI provides limited buffering period for the converter's response to large transients. Therefore, instead of applying traditional PI-based control, fast-dynamic model-predictive control (MPC) was adopted [11, 13].

## III. Model-Predictive Control and Control Saturation in Large Transients

Model-predictive control (MPC) was adopted to manage the fast dynamics of the low-inertia TMVSI. But contrained by the maximum dc-link current and resulted MFT saturation, MPC would suffer saturation issue when the transients are sufficiently large, resulting in oscillation and even instability in the dc-link of the TMVSI. In this section, the MPC is briefly introduced and the control saturation issue will be highlighted to justify the motivation behind the proposed CDC.

### *A. Model-Predictive Control with Feed-Forward Compendation for delays*

In [3], MPPS control was proposed for low-inertia S4T-based MVDC converters. But using a second-order compensation item for computational and sampling delay, it costs lots of computational resources, making it not easily extended to *N*-port LICs ($N \geq 3$). Instead, a new feed-forward compensation (FFC) method with only one single arithmetic operation was proposed in [11] to reduce the computational burden.

Fig. 3 presents the control diagram of the MPC with the computational-inexpensive FFC method. The MPC is implemented in a controller card integrating a digital signal processor (DSP) and field-programmable gate array (FPGA) for each TMVSI module. The DSP was selected to complete floating-point arithmetic with reduced complexity while the FPGA was adopted owing to its superior multitasking performance at an extremely high clock frequency.

Interfacing with the hardware prototype directly, the FPGA accomplishes multiple tasks simultaneously at 50 MHz clock frequency, including sampling and processing voltage/current sensor measurements, detecting overvoltage and overcurrent faults, and executing the state machine for each 16 kHz

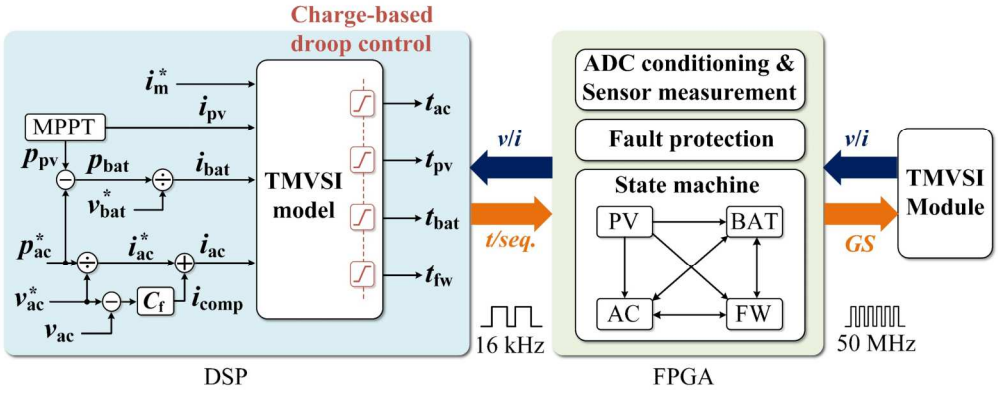


Fig. 3. Control diagram of the proposed charge-based droop control for TMVSI.

switching cycle. Based on sampled data and the TMVSI model, the DSP determines the state sequence and time duration of each state, generating the state machine for each switching cycle. Lastly, the state machine generated in the DSP is sent back to the FPGA to be executed for hardware control. One-switching-cycle computational and sampling delay is induced by this MPC and is compensated by a single arithmetic operation in practive [7, 11].

### *B. Control Saturation Under Large Transients*

The objective of MPC with FFC is to control the dc-link magnetizing current $i_{\mathrm{m}}$ as close to its reference value $I_{\mathrm{m,ref}}$ as possible within each switching cycle, which is dictated by the volt-second balance of magnetizing inductance of the MFT, $L_{\mathrm{m}}$, with

$$i_m = \frac{(V_{pv}\cdot t_{pv}+V_{bat}\cdot t_{bat}+V_{ac}\cdot t_{ac}+V_{fw}\cdot t_{fw})}{L_m} \triangleq i_{\mathrm{m,ref}} \quad (1)$$

$$t_{cal} = t_{pv} + t_{bat} + t_{ac} + t_{fw} + t_{zvs} + t_{res} = T_{sw} \quad (2)$$

In practice, the power mismatch between PV and grid port is balanced out by the decoupling port, the common battery storage/capacitor. With a careful converter design, the calculated time period, $t_{cal}$ always equals to the switching period, $T_{\mathrm{sw}}$, in normal operation.

But under large transients, $t_{cal}$ might exceed $T_{\mathrm{sw}}$, resulting in control saturation. Once control saturation occurs, the time duration of the last active vector, i.e. the AC vector in the example shown in Fig. 2, has to be truncated to maintain a constant switching frequency. Therefore, a power shortage on the AC output and a charge imbalance across $L_{\mathrm{m}}$ would be observed. With only one control of freedom $i_{\mathrm{m}}$, either $i_{\mathrm{m}}$ or $V_{\mathrm{ac}}$ has to be sacrificed, assuming power input is fixed. Since the $L_{\mathrm{m}}$ is designed to allow a current ripple of 0.4~0.6 p.u. for control flexibility, an oscillation on $i_{\mathrm{m}}$ will be observed for a guaranteed $V_{\mathrm{ac}}$ when transients are within the converter limit. Otherwise, the $i_{\mathrm{m}}$ would go above the limit of the MFT and saturate the MFT. As a result, the $L_{\mathrm{m}}$ will drop dramatically and $i_{\mathrm{m}}$ will increase wildly and out of control, leading to a shutdown or catastrophic damage to the converter by overcurrent. This issue deteriorates once LICs are stacked connected such as TMVSI. Fig. 4 presents

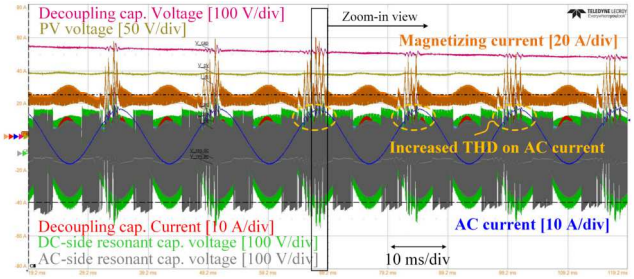


(a)

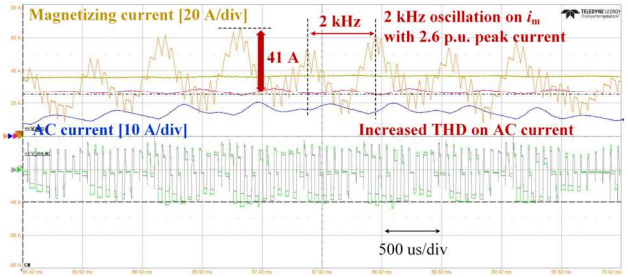


(b)

Fig. 4. 2 kHz oscillation on $i_{\mathrm{m}}$ induced by control saturation in the TMVSI.

the 2 kHz oscillation on $i_{\mathrm{m}}$ under control saturation captured in experiments. The control saturation induced a peak $i_{\mathrm{m}}$ of 2.6 p.u. and increased distortion on AC current of the TMVSI.

To address it, a priority-switching method was proposed in [3]. However, saturation limits on time duration of each state are still required once the $i_{\mathrm{m}}$ goes beyond its design space. Hence, a new anti-windup scheme is desired to address the saturation issue effectively.

## IV. Proposed Charge-Based Droop Control

To address the issue of time saturation while fulfilling the priority-shifting, a charge-based droop control (CDC) is proposed for the low-inertia TMVSI. It can be implemented with either two or three ports since the battery port of the TMVSI provides enhanced flexibility.

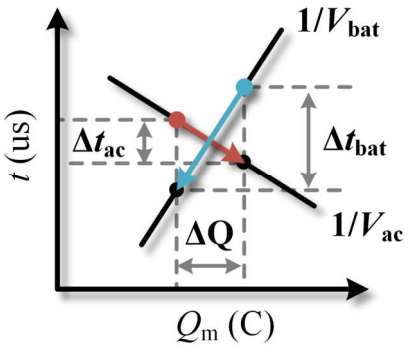


Fig. 5. *Q-t* curves for the proposed charge-based droop control.

As presented in Fig. 3, it shares the same control diagram as the MPC with FFC, expect for an anti-windup scheme for all time durations before sending them to the FPGA to be executed. Analogous to *P-f* droop curve, charge-time $(Q-t)$ curves are defined in the proposed control to eliminate surplus charge in $L_\mathrm{m}$ by sharing the excess time, $\Delta t_{ex}$, by input and output ports. The slopes are determined by voltage magnitudes of charging/discharging vectors.

Fig. 5 illustrates an example of two *Q-t* curves in the proposed CDC, one by the charging battery vector and the other by the discharging AC vector. The horizontal axis represents the accumulated charge in $L_\mathrm{m}$ while the vertical axis the time duration of each state. Once saturation occurs, time periods of both battery and AC vector need to be reduced. For the battery vector, a decrease in time means less charge injected into the $L_\mathrm{m}$ [cf. blue curve in Fig. 5], resulting in a decreased $i_\mathrm{m}$. On the other hand, a reduction in AC state periods indicates less charge consumed from the $L_\mathrm{m}$, i.e., more charge is left in $L_\mathrm{m}$ [cf. red curve in Fig. 5], leading to an increased $i_\mathrm{m}$. Consequently, the time duration changes of these two states should be governed by volt-sec balance across $L_\mathrm{m}$ with (3) so that no oscillation would happen. Finally, $\Delta t_{ex}$ is shared by battery and AC vector with (4).

$$\Delta Q = V_{bat} \cdot \Delta t_{bat} = V_{ac} \cdot \Delta t_{ac} \tag{3}$$

$$\Delta t_{ex} = \Delta t_{bat} + \Delta t_{ac} \tag{4}$$

### A. *Two-Port Approach*

Fig. 6 illustrates the control implementation of the selected state sequence in Fig. 2, where free-wheeling state is ignored for simplicity since it has negligible impact on the charge balance.

In the two-port approach, only battery and AC vectors are involved in eliminating the excess time, $\Delta t_{ex}$, that can be calculated by

$$\Delta t_{ex} = \left(t_{pv} + t_{bat} + t_{ac} + t_{fw} + t_{zvs} + t_{res}\right) - T_{sw} \tag{5}$$

Battery vector, instead of PV vector, is selected to maximize the PV energy revenue for the system.

With (3)(4), the charged balance across $L_\mathrm{m}$ can be guaranteed by

$$\Delta Q = V_{bat} \cdot \Delta t_{bat} = V_{ac} \cdot \Delta t_{ac} = V_{ac} \cdot (\Delta t_{ex} - \Delta t_{bat}) \tag{6}$$

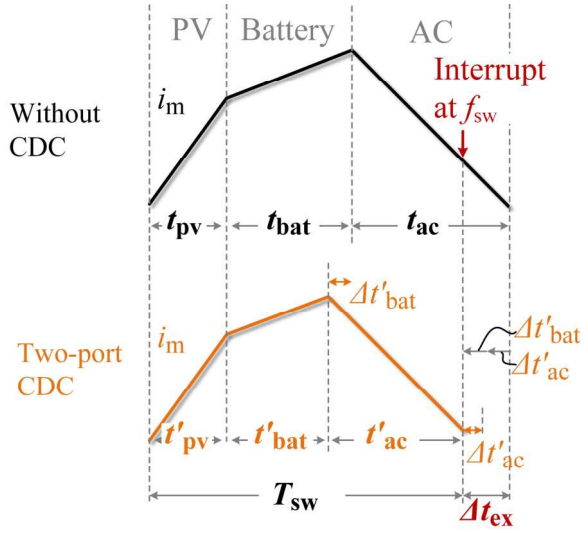


Fig. 6. Two-port implementation for the proposed CDC.

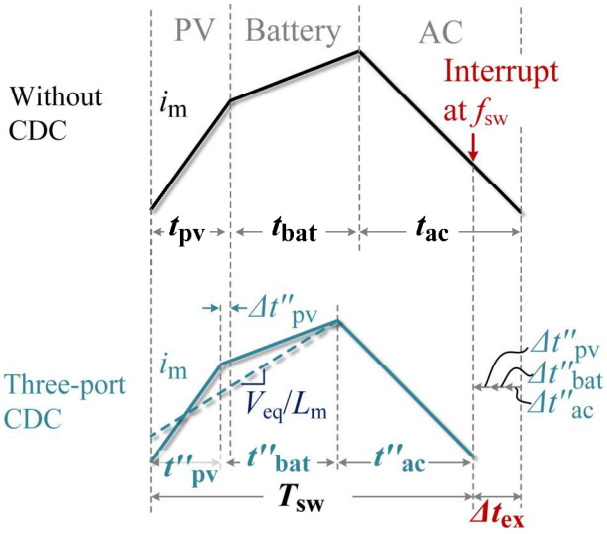


Fig. 7. Three-port implementation for the proposed CDC.

As a result, the total excessive time $\Delta t_{ex}$ can be shared between the battery and AC vector, and the ratio is inverly proportional to their voltage magnitudes. Finally, the new time duration for battery and AC states after anti-windup, $t'_{bat}$ and $t'_{ac}$, can be calculated by

$$t'_{bat} = t_{bat} - \Delta t'_{bat} = t_{bat} - \frac{V_{ac}}{V_{bat}+V_{ac}} \cdot \Delta t_{ex} \tag{7}$$

$$t'_{ac} = t_{ac} - \Delta t'_{ac} = t_{ac} - \frac{V_{bat}}{V_{bat}+V_{ac}} \cdot \Delta t_{ex} \tag{8}$$

### B. *Three-port Approach*

Alternatively, the proposed control can also be fulfilled with three ports by engaging the PV port into the procedure as well.

The three-port approach is implemented in two steps. Firstly, two charging vectors, PV and battery in the selected example

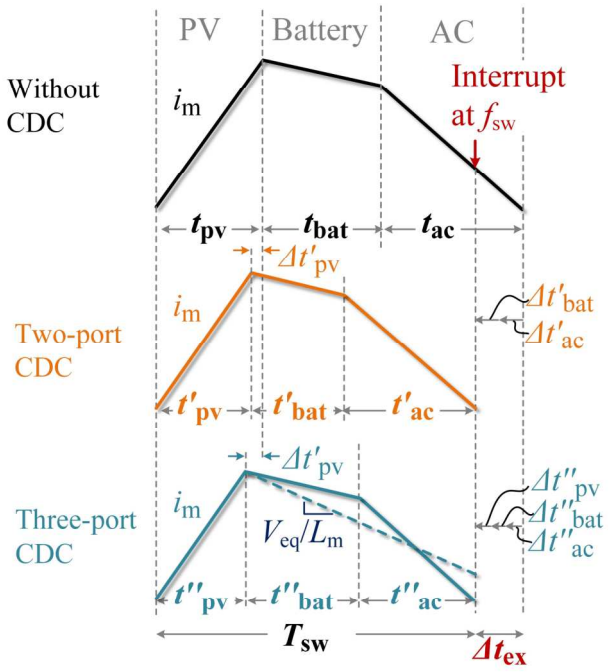


Fig. 8. Two-port and three-port implementation for the proposed CDC in another state sequence with one charging vector (PV) and two discharging vectors (battery and AC).

shown in Fig. 2, are regarded as one equivalent vector, $V_{dc,eq}$, with

$$V_{bat} \cdot t_{bat} + V_{pv} \cdot t_{pv} = V_{dc,eq} \cdot (t_{bat} + t_{pv}) = V_{ac} \cdot t_{ac} \quad (9)$$

This combined DC vector reduces the $\Delta t_{ex}$ along with AC vector in a droop control way with (9) - (11), similar to the two-port approach.

$$\Delta t''_{bat} + \Delta t''_{pv} = \frac{V_{ac}}{V_{dc,eq}+V_{ac}} \cdot \Delta t_{ex} \quad (10)$$

$$t''_{ac} = t_{ac} - \Delta t''_{ac} = t_{ac} - \frac{V_{dc,eq}}{V_{dc,eq}+V_{ac}} \cdot \Delta t_{ex} \quad (11)$$

In the second step, another charge-based droop control is performed on the combined DC vector by PV and battery, which can be achieved with

$$t''_{pv} = t_{pv} - \Delta t''_{pv} = t_{pv} - \frac{V_{bat}}{V_{pv}+V_{bat}} \cdot \frac{V_{ac}}{V_{dc,eq}+V_{ac}} \cdot \Delta t_{ex} \quad (12)$$

$$t''_{bat} = t_{bat} - \Delta t''_{bat} = t_{bat} - \frac{V_{pv}}{V_{pv}+V_{bat}} \cdot \frac{V_{ac}}{V_{dc,eq}+V_{ac}} \cdot \Delta t_{ex} \quad (13)$$

In short, the three-port approach repeats the two-port approach twice, one between combined DC charging vector and the AC discharging vector and the other between the combined DC charging vector itself. This way provides extra flexibility and capability to address the time saturation at the penalty of one more step calculation. Both approaches are universal and can be seamlessly migrated to other state sequences and multi-port LICs with more than three ports.

### C. *Implementation in Another State Sequence with One Charging Vector and Two Discharging Vectors*

In addition to the state sequence shown in Fig. 2, there is another state sequence in the TMVSI, where PV charges the $L_m$ and battery and AC discharge it.

Fig. 8 illustrates the proposed CDC for this state sequence, including both two-port and three-port implementation approaches. In the two-port approach, PV vector has to be used since it is the only charging vector for $L_m$. For the discharging vectors, battery vector is used to minimize the distortion on AC output. In the three-port method, battery and AC vectors are combined as one discharging vector to provide extra capability for saturaton elimination. One more sharing between the battery and AC vector would happen in the second step of three-port CDC implementation.

## V. Simulation Validation

To validate the efficacy of the proposed CDC, a high-fidelity simulation model of the 25 kVA/600 Vac TMVSI module was built in PLECS. All signal latency by control, sensor bandwidth and delay have been included to mimic the hardware prototypes.

Table I summarizes the specifications of the 25 kVA/600 Vac TMVSI module in simulation and Fig. 9 presents the simulation results of the proposed CDC under 50% load step change at AC peak. Without the proposed control, more than 50% surplus time was induced, resulting in a 2 kHz oscillation with 2 p.u. overcurrent on $i_m$, similar to the experimental results shown in Fig. 4. This 2 kHz oscillation significantly increased ripple on the $i_m$ and increased harmonics on AC output.

TABLE I. Specifications of the 25 kVA/600 Vac TMVSI Module in Simulation

| Parameters | Values | Parameters | Values |
|---|---|---|---|
| Rated power | 25 kVA | PV voltage | 1000 Vdc |
| Battery voltage | 650 Vdc | AC voltage | 600 Vac |
| Controlled dv/dt | 1 kV/us | THD of AC output | 3% |
| Switching frequency | 16 kHz | Decoupling capacitor | 1.6 mF |
| Mag. inductance | 340 uH | Saturation current | 170 A |
| Resonant capacitor | 60 nF | Resonant inductor | 2 uH |

In comparison, the proposed CDC in both two-port and three-port implementation approaches addressed the time saturation effectively, reducing the $i_m$ ripple by 75%, peak $i_m$ by 50%. As a result, a well-controlled and low-distorted $i_m$ and AC output were achieved.

## VI. Conclusion

Control saturation is a challenging issue in LICs and would result in undesired oscillation and even instability. In this article, a charge-based droop control is proposed to address this issue in LICs. It can be implemented in either two-port or three-port approaches. A high-fidelity simulation model to mimic the hardware prototype was used to validate the efficacy of the proposed control. In simulation, the proposed scheme

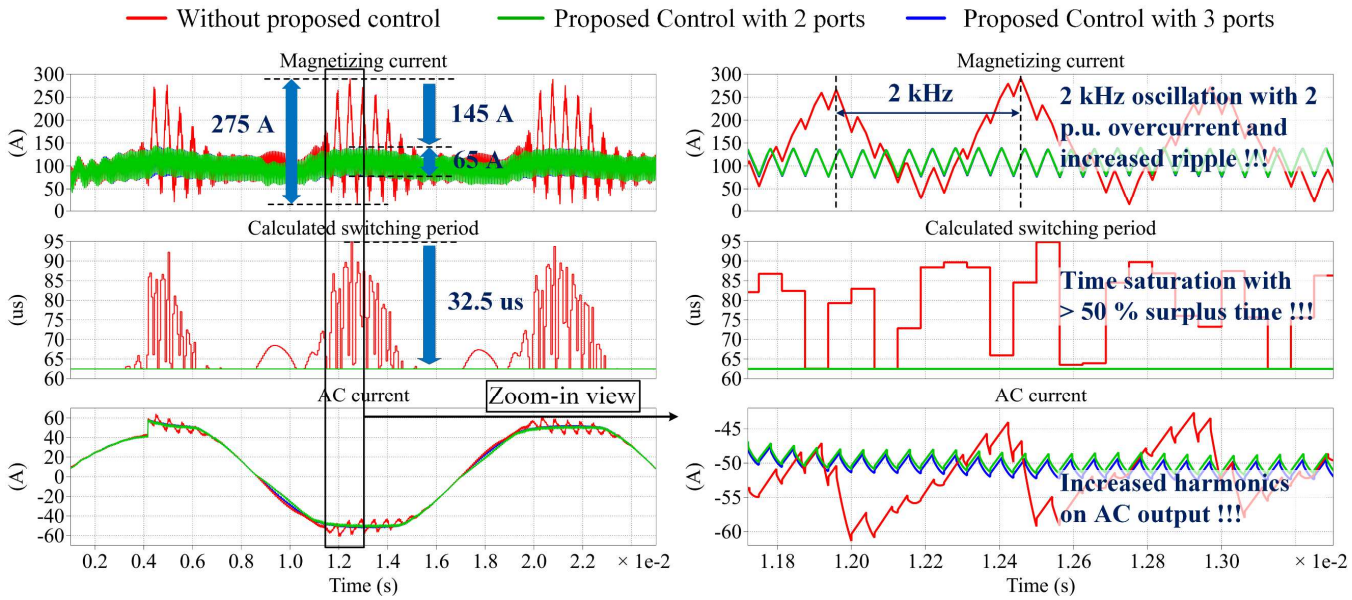


Fig. 9: Simulation results of the proposed CDC to address control saturation under 50% load step change at AC peak. The proposed control eliminates the 2 kHz oscillation by reducing $i_{\mathrm{m}}$ ripple by 75%, peak $i_{\mathrm{m}}$ by 50%.

eliminated the 2 kHz oscillation and reduced the $i_{\mathrm{m}}$ ripple by 75%, $i_{\mathrm{m}}$ overshoot by 50%, leading to a well-controlled and low-distorted $i_{\mathrm{m}}$ and AC output.

## ACKNOWLEDGMENT

This work was supported by the U.S. Department of Energy under the Solar Energy Technologies Office Award DE-EE0008351 and the Center for Distributed Energy at Georgia Tech, Atlanta, GA, USA.

## REFERENCES

[1] D. Divan, Z. An, and P. Kandula, “Soft-switching - The Key to High Power WBG Converters,” *2018 Int. Power Electron. Conf. IPEC-Niigata - ECCE Asia 2018*, no. Figure 1, pp. 4001–4008, 2018.

[2] D. Divan, R. P. Kandula and M. J. Mauger, "The Case for Soft Switching in Four-Quadrant Power Converters," in IEEE Journal of Emerging and Selected Topics in Power Electronics, vol. 9, no. 6, pp. 6545-6560, Dec. 2021.

[3] L. Zheng, R. P. Kandula, K. Kandasamy and D. Divan, "Stacked Low-Inertia Converter or Solid-State Transformer: Modeling and Model Predictive Priority-Shifting Control for Voltage Balance," in IEEE Transactions on Power Electronics, vol. 36, no. 8, pp. 8934-8952, Aug. 2021.

[4] R. Amorim Torres, H. Dai, W. Lee, B. Sarlioglu and T. Jahns, "Current-Source Inverter Integrated Motor Drives Using Dual-Gate Four-Quadrant Wide-Bandgap Power Switches," *IEEE Trans. Ind. Applicat.*, vol. 57, no. 5, pp. 5183-5198, Sept.-Oct. 2021.

[5] M. Guacci et al., "Three-phase two-third-PWM buck-boost current source inverter system employing dual-gate monolithic bidirectional GaN e-FETs," CPSS Trans. Power Electron. Applicat., vol. 4, no. 4, pp. 339-354, Dec. 2019.

[6] H. Chen and D. Divan, "Soft-Switching Solid-State Transformer (S4T)," *IEEE Trans. Power Electron.*, vol. 33, no. 4, pp. 2933-2947, April 2018.

[7] Z. An, X. Han, V. R. Chowdhury, J. Benzaquen, R. P. Kandula and D. Divan, "A Tri-Port Current-Source Soft-Switching Medium-Voltage String Inverter for Large-Scale Solar-Plus-Storage Farms," in IEEE Transactions on Power Electronics, 2022, doi: 10.1109/TPEL.2022.3185006.

[8] L. Zheng et al., "SiC-Based 5-kV Universal Modular Soft-Switching Solid-State Transformer (M-S4T) for Medium-Voltage DC Microgrids and Distribution Grids," in IEEE Transactions on Power Electronics, vol. 36, no. 10, pp. 11326-11343, Oct. 2021.

[9] Y. Xu, Z. Wang, P. Liu, Y. Chen, and J. He, “Soft-Switching Current-Source Rectifier Based Onboard Charging System for Electric Vehicles,” *IEEE Trans. Ind. Applicat.*, 2021.

[10] K. Mozaffari and M. Amirabadi, "A Reduced-Switch-Count Family of Soft-Switched High-Frequency Inductive AC-Link Converters," *IEEE Trans. Power Electron.*, vol. 35, no. 8, pp. 7972-7990, Aug. 2020.

[11] Z. An, R. P. Kandula, and D. Divan, “Feed-Forward Compensation for Model Predictive Control in Tri-port Current-Source Medium-Voltage String Inverters for PV-Plus-Storage Farms,” in *2021 IEEE Energy Conversion Congress and Exposition (ECCE)*, 2021, pp. 3430–3435.

[12] Z. An, R. P. Kandula, and D. Divan, “Comparative Investigation of System-Level Optimized Power Conversion System Architectures to Reduce LCOE for Large-Scale PV-Plus-Storage Farms,” in *2021 IEEE Energy Conversion Congress and Exposition (ECCE)*, 2021, pp. 719–726.

[13] P. Cortes, M. P. Kazmierkowski, R. M. Kennel, D. E. Quevedo and J. Rodriguez, "Predictive Control in Power Electronics and Drives," in IEEE Transactions on Industrial Electronics, vol. 55, no. 12, pp. 4312-4324, Dec. 2008.